



# Impulse Noise Suppression by Deep Learning-Based Receivers in OFDM Systems

Der-Feng Tseng<sup>1</sup> · Che-Shien Lin<sup>1</sup> · Shu-Ming Tseng<sup>2</sup>

Accepted: 27 February 2024 / Published online: 26 March 2024

© The Author(s), under exclusive licence to Springer Science+Business Media, LLC, part of Springer Nature 2024

## Abstract

Orthogonal Frequency Division Multiplexing (OFDM) systems are prone to signal corruption caused by strong and frequent impulses, which can be further exacerbated by multipath fading. Recent evolutions highlight the efficacy of a deep neural network (DNN) receiver in intrinsically estimating channel state information and recovering data explicitly, even without presuming the signal-to-noise ratio (SNR) level. However, the conventional DNN-based receiver, trained on data generated from computer simulations with WINNER II channel model and additive white Gaussian noise (AWGN), is susceptible to substantial performance degradation when subject to impulse noise. To address this challenge, this paper proposes fine-tuning the DNN model using impulse noise-laced data samples during subsequent training. The proposed method aims to enhance representation learning and improve the robustness of the receiver against impulse noise. The efficacy of the DNN-based receiver is assessed by comparing its bit error rate (BER) performance to that of a compressive sensing-based receiver, enabled by the consensus alternating direction method of multipliers (ADMM). Remarkably, the proposed DNN-based receiver achieves BER performance comparable to the clipping-featured receiver, which requires knowledge of the SNR value, an assumption relaxed by our enhanced DNN approach. Furthermore, extensive simulations demonstrate the promising robustness of the deep learning-based approach against impulse noise model mismatches between training and testing scenarios.

**Keywords** Neural network · ADMM · Impulse noise · OFDM · Compressive sensing

---

✉ Der-Feng Tseng  
dtseng@mail.ntust.edu.tw

Che-Shien Lin  
M10707610@mail.ntust.edu.tw

Shu-Ming Tseng  
shuming@ntut.edu.tw

<sup>1</sup> Department of Electrical Engineering, National Taiwan University of Science and Technology, Taipei, Taiwan

<sup>2</sup> Department of Electronic Engineering, National Taipei University of Technology, Taipei, Taiwan

## 1 Introduction

Deep learning (DL) adopts a deep neural network (DNN) to encapsulate data representations at various layers, which could be facilitated through a diverse array of machine learning (ML) techniques such as supervised ML, unsupervised ML, and reinforcement learning. One of the most remarkable DL paradigms in communication systems is the DNN-based codec (i.e., encoder and decoder) presented in [23], which harnesses inherent expressiveness of deep architectures to exhibit competitive system performance to the result driven by communication theory-based algorithms. As a remarkable instance, a data-driven DNN model proposed in [32] indirectly addresses the challenges posed by multipath fading in Orthogonal Frequency Division Multiplexing (OFDM) systems while simultaneously recovering the transmitted symbols, in contrast with the inevitability of channel state information estimation in conventional communication systems receivers; indeed, the findings from extensive simulations highlight that the DNN-based receiver exhibits performance comparable to that of the minimum mean-square error (MMSE) estimator. Alternatively, a model-driven DL approach was presented in [7], where the receiver architecture is composed of two primary entities—a channel estimation subnet and an OFDM signal detection subnet—both realized through DNNs. Further exploration of the DL realm extends to the integration of a deep unfolding approach, as elucidated in [33], demonstrating the effectiveness of applying DL to realize an equalizer in underwater acoustic OFDM systems. An analogous neural networking receiver to tackling issues such as limited pilots and short cyclic prefixes (CPs) was laid out in [17]. A robust DNN-based precoder in massive Multiple Input Multiple Output (MIMO) systems was introduced in [26] to effectively mitigate the harmful effects stemming from imperfect channel state information (CSI).

The quest for optimal performance in communication systems is often hindered by the complex nature of ambient noise present in real-world physical channels. This complexity arises from the difficulty in accurately modeling such noise, leading to received signals of substantial magnitude and unpredictability [5, 21, 24, 31]. The presence of non-Gaussian impulsive noise further compounds this challenge, jeopardizing the guaranteed quality of service typically established under the assumption of a stationary Gaussian random process as the predominant source of interference. A notable example of combating impulsive noise is the application of a fuzzy median filter, as demonstrated in millimeter wave MIMO systems [21]. Adding to that challenge is the inherent vulnerability of DNNs to rare adversarial perturbations [11], including impulsive noise. This prompts a rigorous study on how DNNs can be harnessed to effectively address the negative impact of non-Gaussian noise in communication systems. Drawing inspiration from the domain of image processing, an innovative approach was introduced in [2], leveraging Artificial Intelligent Neural Networks so as to expand feature dimensions to train a fully connected (FC) neural network for binary classification—specifically detecting impulsive occurrences in OFDM blocks. Unlike this approach, our proposed DNN-based receiver, following the pioneering work of [32], obviates the need for the otherwise inevitable multipath fading channel estimation, thereby focusing on the process of explicit data recovery. The realm of OFDM channel estimation under impulsive noise scenarios was explored through a denoising autoencoder DNN in [18]. Additionally, the synergy of a Convolutional Neural Network (CNN) and Long Short-Term Memory (LSTM) was harnessed in [19] to estimate communication channels within spatio-temporal impulsive noise channels; however, enhanced reliability in this context often yields at the cost of using partial channel statistics. In the domain of

power line communication systems, [25] introduced a DNN-based approach for evaluating model parameters, albeit with the inadvertent assumption of an impulse noise model as a Gaussian mixture model (GMM). Analogously, [6] proposed a GMM-based wireless channel estimator trained on imperfect training data. Furthermore, a notable investigation by He et al. [13] delved into a CNN-based learning algorithm tailored for OFDM systems, with an aim at estimating parameters crucial for impulsive noise suppression. Going beyond the scope of FC neural network models, the field of Polar codes drove the application of an LSTM neural network decoder in [30]. This decoder adeptly addresses memory impulse noise, exhibiting superior system performance and latency results compared to established decoding techniques. Notably, multipath fading channels were not considered in those systems studied in [13, 25, 30].

This paper presents an in-depth analysis of the impact of impulse noise on the bit error rate (BER) performance of a DNN-based receiver in OFDM systems undergoing multipath fading channels. Notably, the DNN-based receiver operates without prior knowledge of impulse statistics, fading coefficients, or the Signal-to-Noise Ratio (SNR) level. Our approach involves a two-stage training process: the initial stage involves modeling OFDM signaling within fading channels, simulated based on specific channel statistics in AWGN. The subsequent stage fine-tunes the model by integrating training data infused with impulse noise. This sophisticated DNN model aims to mitigate the detrimental impact of impulse noise across all subcarriers, a challenge often overlooked yet critical for robust data recovery. Remarkably, even in the face of inherent disparities between training and testing datasets, our experimental outcomes substantiate the efficacy of our approach in combating the adverse effects of impulse noise on data recovery. This further reinforces the resilience of our proposed DNN-based receiver. Beyond harnessing the power of deep learning for targeted impulse noise attenuation, our work importantly establishes a crucial connection between optimal clipping thresholds—quintessential in governing the BER performance of clipping-featured receivers facing impulse noise—and a computationally efficient resolution of this challenge via second-order cone programming (SOCP) formulation. To pursue this optimization solution in a distributed manner, we employ the consensus alternating direction method of multipliers (ADMM) algorithm [3]. Particularly noteworthy is the fact that the conventional clipping-featured receiver relies on the SNR level to calibrate the clipping threshold judiciously. However, as highlighted in [28], its efficacy in suppressing impulse noise becomes compromised when the threshold is measured amidst substantial deviations from the true SNR value. In contrast, our subsequent BER performance comparison—benchmarked against the performance achieved through convex programming introduced in [4]—serves as a compelling evidence to the effectiveness of our DNN-based receiver. Intriguingly, our DNN-based receiver excels while circumventing the reliance on assumed SNR levels and CSI, thereby emphasizing its pragmatic adaptability.

The contribution of this paper is highlighted in the following list:

- In pursuit of a versatile model adaptable to diverse real-world scenarios, we advance the training paradigm of a pre-trained DNN by incorporating the principles of representation learning. This strategic enhancement entails refining the model's efficacy through the integration of impulse noise-laced training data in the secondary training stage. This innovation empowers the DNN's adaptability to unforeseen impulse noise challenges, a cornerstone for robust communication performance.
- Diverging from the system described in [32], we judiciously incorporate inter-block interference into the framework via an additional CP. This strategic inclusion underpins

our effort to synergize impulse noise mitigation with OFDM data detection, which we ingeniously formulate as a convex optimization problem. This formulation culminates in the emergence of a second-order cone programming approach, elegantly addressing the impulse noise corruption.

- Building on the above formulation, our research contributes a meticulous exposition of the consensus ADMM algorithm’s application. Our approach harnesses the efficiency of this algorithm to derive optimal solutions.
- We rigorously subject the trained DNN-based receiver to diverse impulse noise contexts, revealing its robustness against the challenges posed by impulse noise and noise model mismatches under specific conditions. Notably, the BER performance of our DNN receiver closely aligns with its conventional clipping-featured counterpart, a benchmark receiver assuming the knowledge of critical impulse noise model parameters.

This paper is organized as follows: the problem statement and the system framework are reviewed in Sect. 2 subsequently, and the details of the proposed schemes are manifested in Sect. 3. Section 4 will present the simulation results, in terms of bit error rate, and a conclusion is drawn in Sect. 5.

*Notation:* The Hermitian operator is denoted by  $(\cdot)^H$ . For a complex-valued  $x$ , the real and imaginary parts are defined as  $\Re\{x\}$  and  $\Im\{x\}$ , respectively. The indicator function  $\mathbb{1}(y)$  returns one if the condition  $y$  is satisfied and zero otherwise. The  $\ell_2$ -norm of an  $N$ -by-1 vector  $\mathbf{x}$  is expressed as  $\|\mathbf{x}\|_2 = (\sum_{k=1}^N |x_k|^2)^{\frac{1}{2}}$ . Referencing the  $i$ -th element of vector  $\mathbf{u}$  is conventionally accomplished by using  $(\mathbf{u})_i$ .

## 2 System Model

### 2.1 OFDM Block Formation and Fading Channel Modeling

The input bit stream is initially divided into groups based on the alphabet size of Quadrature Phase Shift Keying (QPSK) modulation, assuming Gray mapping. These partitions are then passed through the QPSK modulator, resulting in output symbols denoted as  $X_m$ . Here, the superscript  $m$  signifies the QPSK symbol index, which corresponds to two-bit partition  $\mathbf{u}_m = [(\mathbf{u}_m)_2 \ (\mathbf{u}_m)_1]$ . Refer to Fig. 1 for a visual representation of the process. Once  $N$  modulated symbols are collected, they are arranged into a vector  $\mathbf{X} = [X_0, X_1, \dots, X_{N-1}]^T$ . Let us define  $\omega_N = e^{-j2\pi/N}$ , where  $j$  is the imaginary unit. The Fast Fourier Transform (FFT) matrix  $\mathbf{F}$  (of size  $N \times N$ ) is formulated as follows:

$$\mathbf{F} = \begin{bmatrix} 1 & 1 & 1 & \dots & 1 \\ 1 & \omega_N & \omega_N^2 & \dots & \omega_N^{N-1} \\ 1 & \omega_N^2 & \omega_N^4 & \dots & \omega_N^{2(N-1)} \\ \vdots & \vdots & \vdots & \ddots & \vdots \\ 1 & \omega_N^{N-1} & \omega_N^{2(N-1)} & \dots & \omega_N^{(N-1)^2} \end{bmatrix}. \tag{1}$$

After undergoing an Inverse FFT (IFFT), the time-domain signal block  $\mathbf{x} = [x_0, x_1, \dots, x_{N-1}]^T$  can be written as follows:

$$\mathbf{x} = \mathbf{F}^H \mathbf{X}. \tag{2}$$

Specifically, the element  $x_k$  is expressed by the following:

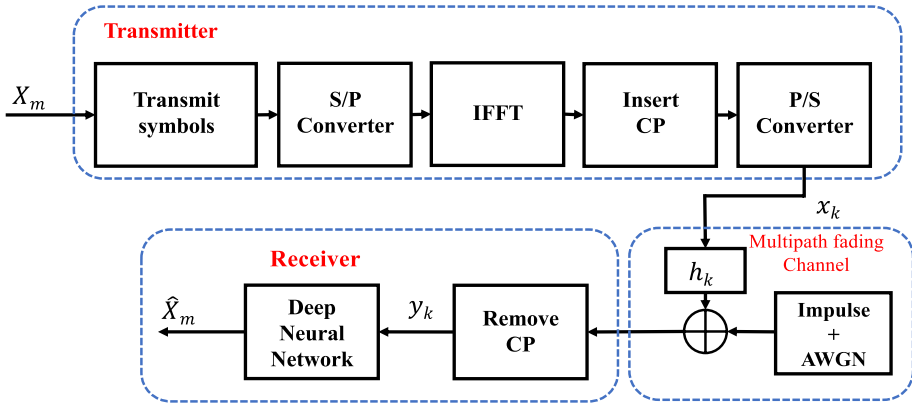


Fig. 1 OFDM System model

$$x_k = \frac{1}{\sqrt{N}} \sum_{m=0}^{N-1} X_m e^{j\frac{2\pi mk}{N}}, \quad k \in \{0, 1, \dots, N - 1\}, \tag{3}$$

where  $m$  is the sub-carrier index for the IFFT implementation (over which the symbol  $X_m$  is transported) and  $N$  is the IFFT size. For a sufficiently large IFFT size  $N$ , the temporal sequence  $x_k$  ( $0 \leq k \leq N - 1$ ) is modeled by an independent, identically distributed (*i.i.d.*) Gaussian random vector, with each entry  $x_k$  characterized by a mean of zero and a variance of  $E_s$ —which is identical to the modulated symbol energy, i.e.,  $E(|X_m|^2)$  for all  $m$ —by invoking the central limit theorem.

To preempt inter-block interference, the insertion of a CP is executed at the output of the parallel-to-serial converter. This CP, with a length denoted as  $\mathcal{L}_p$ , is intentionally chosen to exceed the delay spread of the multipath fading channel, ensuring  $\mathcal{L}_p \geq L$ . The Channel Impulse Response (CIR) characterizing the effect on the OFDM symbol is succinctly encapsulated by a CIR vector, represented as follows

$$\mathbf{h} = [h_0, h_1, \dots, h_{L-1}]. \tag{4}$$

Given the premise of precise time and frequency synchronization at the receiver, the intricate time-domain representation of the received signal sequence, after removal of the CP, can be elegantly captured as:

$$r_k = h_k \otimes x_k = r_{k_I} + jr_{k_Q} \quad (0 \leq k \leq N - 1). \tag{5}$$

In this context, the operator  $\otimes$  is used to denote the  $N$ -point circular convolution. At each discrete time instance indexed by  $k$ , the in-phase and quadrature-phase components of the received signal  $r_k$  are represented as  $r_{k_I}$  and  $r_{k_Q}$ , respectively. To account for the additive interference, the sequence of received signals is expressed as  $y_k = h_k \otimes x_k + \eta_k$ . The term  $\eta_k$  encompasses noise contributions originating from diverse sources, as elaborated upon in the following:

$$\eta_k = i_k + \xi_k. \tag{6}$$

Here,  $\xi_k$  symbolizes the AWGN, characterized by a flat single-sided power spectral density (PSD) with amplitude  $N_0$ . Moreover, the subsequent subsection delves into the formulation of the remaining impulse noise term  $i_k$ .

### 2.2 Memoryless Impulse Noise Modeling

One of the most popularly used statistical models to construct the memoryless impulse noise is the GMM. For instance, Bernoulli-Gaussian (B-G) model [8], where, in addition to AWGN, the impulse occurrence  $i_k = b_k \tilde{i}_k$  is taken into account and characterized by an inherent Bernoulli random variable  $b_k \in \{0, 1\}$  with the probability of impulse occurrence denoted by  $P(b_k = 1) = p_b$ . Further, the impulse noise sequence  $\tilde{i}_k (k = 0, \dots, N - 1)$  is also an independent and identically distributed (*i.i.d.*) Gaussian random process with mean zero and variance  $\frac{N_0}{2}\Gamma$  (per dimension), where the impulse-to-Gaussian ratio  $\Gamma$ , a strength indicator of the impulse noise, is the mean power ratio between the impulse noise  $\tilde{i}_k$  and the AWGN noise  $\xi_k$ , and abbreviated by IGR. As a consequence, the probability density function (PDF) of the noise sample  $\eta_k$  (a two-state Gaussian mixture model) is written as follows:

$$P_{\eta_k}^{BG}(x) = (1 - p_b) \mathcal{CN}(x;0, N_0) + p_b \mathcal{CN}(x;0, N_0(1 + \Gamma)) , \tag{7}$$

where

$$\mathcal{CN}(z; \mu_z, \sigma_z^2) = \frac{1}{\pi \sigma_z^2} e^{-\frac{|z-\mu_z|^2}{\sigma_z^2}}$$

is the PDF of a circular symmetric Gaussian random variable  $z$ , the mean and variance of which are denoted by  $\mu_z$  and  $\sigma_z^2$ , respectively. From the description of the noise model in (7), it is worth noting that sophisticated receivers require precise knowledge of the underlying model parameters such as  $p_b$ ,  $\Gamma$ , and  $N_0$  to realize system performance gain. Another widely adopted GMM but with infinite states is Middleton Class-A (MC-A) noise model [20]. The PDF of the *i.i.d.* noise sample  $\eta_k$  is expressed as follows:

$$P_{MC-A}(x) = \sum_{\ell=0}^{\infty} \alpha_{\ell} \mathcal{CN}(x;0, \varphi_{\ell}) , \tag{8}$$

where  $\alpha_{\ell} = e^{-A} \frac{A^{\ell}}{\ell!}$  and  $\varphi_{\ell} = N_0(1 + \frac{\ell}{\Lambda A})$ . Typically,  $A$  is referred to as the *impulsive index* and  $\Lambda$  is the ratio between the AWGN's mean power, and that of the impulsive noise.

Aside from the aforementioned Gaussian mixture models, the symmetric alpha-stable (*S $\alpha$ S*) distribution [22], defined by the following characteristic function

$$\varphi(t) = e^{-\gamma|t|^{\alpha}} , \tag{9}$$

is commonly used as well, where the characteristic exponent  $\alpha (0 < \alpha \leq 2)$  intimates the degree of impulsiveness: the PDF induced by the *S $\alpha$ S* distribution is yielded by the inverse Fourier transform of (9), as expressed in the following:

$$P(x; \alpha, \gamma) = \frac{1}{2\pi} \int_{-\infty}^{\infty} \varphi(t) e^{-jtx} dt = \frac{1}{2\pi} \int_{-\infty}^{\infty} e^{-(\gamma|t|^{\alpha} + jtx)} dt . \tag{10}$$

Empirically, a smaller  $\alpha$  signifies more impulsive behavior and vice versa. The particular case with  $\alpha = 2$  corresponds to Gaussian distribution while Cauchy distribution is associated with the special setting of  $\alpha = 1$ . A scale parameter  $\gamma$  ( $\gamma > 0$ ) is in regards to driving the dispersion; for instance, the variance of Gaussian distribution ( $\alpha = 2$ ) is measured by  $2\gamma$ . Since the variance of this impulse noise distribution is infinite—thanks to its heavy tails in the context of  $\alpha < 2$ , the geometric signal-to-noise ratio (G-SNR), defined as

$$\text{G-SNR} = \frac{1}{2C_g} \left( \frac{A_0}{C_g^{\frac{1}{\alpha}-1} \gamma^{\frac{1}{\alpha}}} \right)^2, \tag{11}$$

is a metric substituting for SNR. Moreover,  $A_0 = 1$  and  $C_g \approx 1.78$  are used in (11) [10].

It is imperative to stress that the proposed DNN-based receiver, devoid of prior knowledge regarding the specific impulse noise model under consideration, is purposefully subjected to testing. This approach, resonant with real-world scenarios, underscores the resilience of our receiver against the unexpected variability in impulse noise models. Subsequently, the entailing BER performance results (refer to Sect. 4) reinforce its remarkable adeptness in mitigating the adverse effects of impulse noise, notwithstanding the pervasive presence of model mismatches.

### 2.3 Compressive-Sensing Based Receiver

This subsection initiates by shedding light on the viability of a benchmark receiver rooted in compressive sensing, strategically applied within impulse-corrupted OFDM systems. A notable facet of this benchmark involves harnessing consensus Alternating Direction Method of Multipliers (ADMM), a paradigm of distributed processing. Delving into the mechanics of this framework, we subsequently elucidate its derivation. Notably, the efficacy of this benchmark receiver thrives contingent upon the availability of CSI and SNR level—a caveat intrinsic to this compressive-sensing based receiver. Ultimately, we will assess the efficacy of our proposed DNN-based receiver through extensive computer simulations. We will compare its performance with that of the compressive-sensing based counterpart in terms of BER.

In accordance with established conventions (cf. (6)), the impulse noise instances are collocated and structured into a vector format denoted as  $\mathbf{i} = [i_0, i_1, \dots, i_{N-1}]^T$ . Similarly, the AWGN noise samples are organized as  $\boldsymbol{\xi} = [\xi_0, \dots, \xi_{N-1}]^T$ . Successively, the vector form of the received signal sequence can be analogously written as follows:

$$\mathbf{y} = \mathbf{H}\mathbf{x} + \boldsymbol{\eta}, \tag{12}$$

where the composite non-Gaussian interference vector is represented by

$$\boldsymbol{\eta} = \mathbf{i} + \boldsymbol{\xi}, \tag{13}$$

and  $\mathbf{H}$  denotes an  $N$ -by- $N$  circulant matrix with the transposed form of  $\mathbf{h}$  (cf. (4)) serving as its first column. The concatenated output of the IFFT is represented as  $\mathbf{x} = [x_0, \dots, x_{N-1}]^T$ . It is crucial to emphasize that achieving robust OFDM detection against gross errors through  $\ell_1$ - $\ell_2$  optimization [4] cannot be guaranteed solely based on an isolated OFDM block (subsequent to CP removal). This limitation emerges due to the inherent deficiency in the rank of the  $N$ -by- $N$  matrix  $\mathbf{H}$ , which is formed using elements that are randomly generated. Furthermore, in contrast to the strategy presented in [1], which relies on null subcarriers exclusively reserved for sparse signal recovery as a means to overcome this

dimensional challenge, the proposed benchmark receiver directly addresses the broader context of impulse noise mitigation in generic OFDM transmission. Of paramount importance, the proposed approach does not hinge on a specific estimation phase and is not contingent upon the use of reserved null subcarriers, as highlighted in [1].

Recall that the DNN receiver developed in [32] considers a data transmission frame comprising two distinctive OFDM blocks. The first block is exclusively composed of pilot symbols, while the second is allocated for the transmission of actual data. Importantly, the CIR is assumed not to vary within the time span of a frame. However, rather than discarding the potentially valuable information embedded within, the innovative impulse noise mitigation approach introduced in this paper takes a step further by exploiting the corrupted CP-length signals situated between the two OFDM blocks. This strategic incorporation serves as a countermeasure against the rank deficiency challenges typically encountered in compressive sensing scenarios. It is worth noting that a similar mechanism was employed in [27], although its application was limited to scenarios involving AWGN. In congruence with the architecture outlined in [27], and harnessing this additional CP segment to avert rank deficiency issues, it is of utmost significance to underscore that this section of the paper (distinctively disregarded in preceding studies such as [27]) is dedicated to the realization of impulse noise mitigation through the prism of convex programming. Notably, the forthcoming passages provide a meticulous delineation of the relevant mathematical notations.

The  $p$ -th transmission frame is defined by two consecutive OFDM blocks:  $\mathbf{X}(2p)$  and  $\mathbf{X}(2p + 1)$ , identified by their indices as  $(2p)$  and  $(2p + 1)$ , respectively. Analogously, the  $(2p)$ -th received signal block, subsequent to CP removal, is expressed as follows:

$$\mathbf{y}(2p) = \mathbf{H}_T \mathbf{I}_E \mathbf{x}(2p) + \boldsymbol{\eta}(2p), \tag{14}$$

where the time-domain signal vector is encapsulated as  $\mathbf{x}(2p) = \mathbf{F}^H \mathbf{X}(2p)$ , and the matrix  $\mathbf{H}_T$  is structured as a  $N$ -by- $(N + \mathcal{L}_p)$  Toeplitz matrix, with the first row corresponding to the CIR vector  $[\mathbf{h}, 0, \dots, 0]$ , while the first column marked by  $[h_0, 0, \dots, 0]^T$ . To seamlessly integrate the concept of CP insertion with the underlying OFDM block, a crucial step entails the construction of the  $(N + \mathcal{L}_p)$ -by- $N$  matrix  $\mathbf{I}_E$ . This is accomplished by appending a submatrix  $\tilde{\mathbf{I}}_{\mathcal{L}_p}$  beneath an  $N$ -by- $N$  identity matrix  $\mathbf{I}_N$ , where  $\tilde{\mathbf{I}}_{\mathcal{L}_p}$  is crafted through the extraction of the initial  $\mathcal{L}_p$  rows from  $\mathbf{I}_N$ . This intricate process culminates in the synthesis of the composite matrix  $\mathbf{I}_E = [\mathbf{I}_N^T \tilde{\mathbf{I}}_{\mathcal{L}_p}^T]^T$  in (14).

As opposed to the utilization of a single OFDM block-time observation, as implicated in (14), this paper considers the signal sequence with respect to the  $p$ -th transmission frame, which now extends in length to  $M \triangleq 2N + \mathcal{L}_p$  instead of  $2N$ . This sequence is expressed in vector form as follows:

$$\begin{aligned} \bar{\mathbf{y}}_f(p) &= \bar{\mathbf{H}}_T \bar{\mathbf{I}}_E \bar{\mathbf{x}}(p) + \bar{\boldsymbol{\eta}}(p) \\ &= \Xi \bar{\mathbf{x}}(p) + \bar{\boldsymbol{\eta}}(p), \end{aligned} \tag{15}$$

where the matrix  $\bar{\mathbf{H}}_T$  takes on the form of a  $M \times (M + \mathcal{L}_p)$  Toeplitz matrix. The first row is represented by  $[\mathbf{h}, 0, \dots, 0]$  of size  $M$ , and first column adopts the configuration  $[h_0, 0, \dots, 0]^T$  of size  $(M + \mathcal{L}_p)$ . Simultaneously, the matrix  $\bar{\mathbf{I}}_E = \mathbf{I}_2 \otimes \mathbf{I}_E$  is an expansion of  $\mathbf{I}_E$  as defined in (14), encompassing a two-by-two identity matrix  $\mathbf{I}_2$  and the Kronecker product denoted by  $\otimes$ . Stacking two transmitted signal blocks yields a tall vector  $\bar{\mathbf{x}}(p) = [\mathbf{x}^T(2p + 1) \ \mathbf{x}^T(2p)]^T$ ; accordingly, the additive noise sequence in regards to the  $p$ -th frame can be represented as another tall vector  $\bar{\boldsymbol{\eta}}(p)$ , which is further decomposed into  $\bar{\boldsymbol{\eta}}(p) = \bar{\mathbf{i}}(p) + \bar{\boldsymbol{\xi}}(p)$ .



Crucially, in the absence of interference, the composite channel matrix (presented as a tall matrix) denoted by  $\Xi = \overline{H}_r \overline{I}_e$  enables the representation of the received sequence as a simple product of  $\Xi$  and the transmission frame  $\overline{\mathbf{x}}(p)$  (refer to (15)). This lays the groundwork for the formulation of the subsequent convex optimization problem. Of notable significance is the incorporation of inter-block interference amidst two consecutive OFDM block-time observations, a distinct hallmark setting the formation (15) apart from the architecture presented in [32]. This distinctive inclusion essentially paves the way for the implementation of a compressive sensing-based receiver in the ensuing discourse.

Leveraging the underpinning structure outlined in (15) and its resonance with sparse impulse noise (gross errors), a strategy rooted in second order cone programming (SOCP) strategy [4] is harnessed to facilitate the recovery of the transmitted signal vector  $\overline{\mathbf{x}}(p)$ . This task can be expressed by the subsequent formulation:

$$\begin{aligned} \min_{\overline{\mathbf{x}}(p), \tilde{\xi}(p)} \quad & \|\overline{\mathbf{y}}_f(p) - \Xi \overline{\mathbf{x}}(p) - \tilde{\xi}(p)\|_1 \\ \text{subject to} \quad & \|\tilde{\xi}(p)\|_2 \leq \lambda; \Xi^H \tilde{\xi}(p) = \mathbf{0}. \end{aligned} \tag{16}$$

Given the potential proliferation of the unknown variables at hand, the endeavor to estimate the OFDM signal vector  $\overline{\mathbf{x}}(p)$  in conjunction with the AWGN noise vector  $\tilde{\xi}(p)$  can be a computationally demanding task. To alleviate this computational burden, a series of mathematical transformations are invoked, as detailed in the following discourse.

It becomes evident that the null space of the tall matrix  $\Xi$  featured in (15) is indeed present. From this perspective, the column space of  $\Xi$  is effectively denoted as  $U$ , while the complementary orthogonal space is represented as  $U^\perp$ . Furthermore, the establishment of an orthobasis for the column space  $U^\perp$  manifests as the matrix  $Q$ . In consequence, the orthonormal projector onto  $U^\perp$  can be succinctly expressed as  $P_{U^\perp} = QQ^H$ . In this regard, the SOCP (as presented in (16)) can be alternatively formulated as follows:

$$\begin{aligned} \min_{\tilde{\mathbf{i}}(p)} \quad & \|\tilde{\mathbf{i}}(p)\|_1 \\ \text{subject to} \quad & \|Q^H(\overline{\mathbf{y}}_f(p) - \tilde{\mathbf{i}}(p))\|_2 \leq \lambda. \end{aligned} \tag{17}$$

Notably, the equivalence between (16) and (17) hinges on the deliberate pursuit of impulse noise mitigation. This is predominantly realized through the initial step of pre-multiplying the received signal vector  $\overline{\mathbf{y}}_f(p)$  by the matrix  $Q^H$ . The resolution of the SOCP problem depicted in (16) can be facilitated by employing the widely utilized CVX [12] software package, as exemplified in [29]. In marked contrast, this paper focuses on incorporating the consensus ADMM-based distributed optimization algorithm [3] as the backbone for implementing impulse noise suppression. This novel approach harnesses its inherent parallelism to enhance convergence speed by strategically decomposing the optimization problem into a series of sub-problems. The ensuing mathematical derivation intricately unfolds in the following passages.

In the first hand, two auxiliary variables  $z_1$  and  $z_2$  are introduced to enable the parallelism for solving (17), as written in the following:

$$\begin{aligned}
 & \min_{\tilde{\mathbf{i}}(p)} \|\tilde{\mathbf{i}}(p)\|_1 \\
 & \text{subject to} \quad \|\mathbf{z}_1\|_2 \leq \lambda \\
 & \quad \mathbf{z}_1 = \mathbf{Q}^H(\bar{\mathbf{y}}_F(p) - \mathbf{z}_2) \\
 & \quad \mathbf{z}_2 = \tilde{\mathbf{i}}(p).
 \end{aligned} \tag{18}$$

Given the *global* variable  $\mathbf{z}_2$ , the *local* variables  $\{\tilde{\mathbf{i}}(p), \mathbf{z}_1\}$  are considered as a group to be optimized, reflecting the essence of implementing the consensus ADMM. In regards to the newly formulated optimization problem by (18), the augmented Lagrangian is laid out as follows:

$$\begin{aligned}
 L_\rho(\tilde{\mathbf{i}}(p), \mathbf{z}_1, \mathbf{z}_2, \boldsymbol{\mu}_1, \boldsymbol{\mu}_2) = & \|\tilde{\mathbf{i}}(p)\|_1 + \boldsymbol{\mu}_1^H(\mathbf{z}_1 - \mathbf{Q}^H(\bar{\mathbf{y}}_F(p) - \mathbf{z}_2)) \\
 & + \frac{\rho}{2} \|\mathbf{z}_1 - \mathbf{Q}^H(\bar{\mathbf{y}}_F(p) - \mathbf{z}_2)\|_2^2 + \boldsymbol{\mu}_2^H(\mathbf{z}_2 - \tilde{\mathbf{i}}(p)) \\
 & + \frac{\rho}{2} \|\mathbf{z}_2 - \tilde{\mathbf{i}}(p)\|_2^2,
 \end{aligned} \tag{19}$$

where  $\rho > 0$  is the penalty parameter, and  $\boldsymbol{\mu}_1$  and  $\boldsymbol{\mu}_2$  are dual variables.

The scaled dual form of ADMM execution is carried out by setting  $\boldsymbol{\omega}_i = \boldsymbol{\mu}_i/\rho$  for  $i \in \{1, 2\}$ . After  $\gamma$  iterations (a positive integer  $\gamma \geq 1$ ), the update for the  $i$ -th entry of impulse noise vector estimate  $\tilde{\mathbf{i}}(p)$ , i.e.,  $(\tilde{\mathbf{i}}(p))_i$  for  $i \in \{1, 2, \dots, M\}$  is yielded—in closed form—by the following:

$$(\tilde{\mathbf{i}}^{\gamma+1}(p))_i = \max \left\{ 0, |(z_2^\gamma + \boldsymbol{\omega}_2^\gamma)_i| - \frac{1}{\rho} \right\} \frac{(z_2^\gamma + \boldsymbol{\omega}_2^\gamma)_i}{|(z_2^\gamma + \boldsymbol{\omega}_2^\gamma)_i|}, \tag{20}$$

Successively, the update for  $\mathbf{z}_1$ —by minimizing (19) while subjecting  $\|\mathbf{z}_1\|_2$  to within the Euclidean ball  $\|\mathbf{z}_1\|_2 \leq \lambda$ —can be yielded in closed formed, and the result is expressed as follows:

$$\mathbf{z}_1^{\gamma+1} = \begin{cases} \mathbf{Q}^H(\bar{\mathbf{y}}_F(p) - \mathbf{z}_2^\gamma) - \boldsymbol{\omega}_1^\gamma, & \text{if } \|\mathbf{Q}^H(\bar{\mathbf{y}}_F(p) - \mathbf{z}_2^\gamma) - \boldsymbol{\omega}_1^\gamma\|_2 \leq \lambda \\ \lambda \frac{\mathbf{Q}^H(\bar{\mathbf{y}}_F(p) - \mathbf{z}_2^\gamma) - \boldsymbol{\omega}_1^\gamma}{\|\mathbf{Q}^H(\bar{\mathbf{y}}_F(p) - \mathbf{z}_2^\gamma) - \boldsymbol{\omega}_1^\gamma\|_2}, & \text{if } \|\mathbf{Q}^H(\bar{\mathbf{y}}_F(p) - \mathbf{z}_2^\gamma) - \boldsymbol{\omega}_1^\gamma\|_2 > \lambda. \end{cases} \tag{21}$$

With the availability of updates  $\tilde{\mathbf{i}}^{\gamma+1}(p)$  as well as  $\mathbf{z}_1^{\gamma+1}$ , the proceeding of ADMM is carried out continually and the global variable  $\mathbf{z}_2$  is updated by the following:

$$\mathbf{z}_2^{\gamma+1} = (\mathbf{Q}\mathbf{Q}^H + \mathbf{I})^{-1} \left( \mathbf{Q}(\mathbf{Q}^H\bar{\mathbf{y}}_F(p) - \mathbf{z}_1^{\gamma+1}) + \tilde{\mathbf{i}}^{\gamma+1}(p) - \mathbf{Q}\boldsymbol{\omega}_1^\gamma - \boldsymbol{\omega}_2^\gamma \right), \tag{22}$$

where the local variables  $\{\tilde{\mathbf{i}}(p), \mathbf{z}_1\}$  are updated by the latest iterates, as shown in (20) and (21), respectively. Finally, the two dual variables  $\boldsymbol{\omega}_1$  and  $\boldsymbol{\omega}_2$  are updated in the following:

$$\boldsymbol{\omega}_1^{\gamma+1} = \boldsymbol{\omega}_1^\gamma + (\mathbf{z}_1^{\gamma+1} - \mathbf{Q}^H(\bar{\mathbf{y}}_F(p) - \mathbf{z}_2^{\gamma+1})) \tag{23}$$

$$\boldsymbol{\omega}_2^{\gamma+1} = \boldsymbol{\omega}_2^\gamma + (\mathbf{z}_2^{\gamma+1} - (\tilde{\mathbf{i}}(p))_i^{\gamma+1}) \tag{24}$$

Denote the primal solutions by  $\tilde{\mathbf{i}}^*(p)$ ,  $\mathbf{z}_1^*$  and  $\mathbf{z}_2^*$ ; likewise, the dual solutions are indicated by  $\boldsymbol{\omega}_1^*$  and  $\boldsymbol{\omega}_2^*$ . As expressed by the following, the necessary and sufficient optimality condition for the ADMM problem (17) are primal feasibility:

$$\begin{aligned} \mathbf{z}_1^* - \mathbf{Q}^H(\bar{\mathbf{y}}_f(p) - \mathbf{z}_2^*) &= 0 \quad \text{where} \quad \|\mathbf{z}_1^*\|_2 \leq \lambda \\ \mathbf{z}_2^* - \tilde{\mathbf{i}}^*(p) &= 0, \end{aligned} \tag{25}$$

and dual feasibility:

$$\begin{aligned} \mathbf{0} &\in \partial\|\tilde{\mathbf{i}}(p)\|_1 - \rho\boldsymbol{\omega}_2^*, \\ \mathbf{0} &\in \mathbf{Q}\boldsymbol{\omega}_1^* + \boldsymbol{\omega}_2^* \end{aligned} \tag{26}$$

where  $\partial(\cdot)$  indicates the subdifferential operator.

The stopping criterion for the consensus ADMM is contrived by first measuring the primal and dual residuals; in a fashion similar to [3], one can obtain the primal residual as follows:

$$\begin{aligned} \zeta_1^\gamma &= \mathbf{z}_1^\gamma - \mathbf{Q}^H(\bar{\mathbf{y}}_f(p) - \mathbf{z}_2^\gamma) \\ \zeta_2^\gamma &= \mathbf{z}_2^\gamma - (\tilde{\mathbf{i}}(p))_i^\gamma \end{aligned} \tag{27}$$

Noteworthy, the iterate  $\mathbf{z}_2^{\gamma+1}$  aims to minimize  $L_\rho(\tilde{\mathbf{i}}^{\gamma+1}(p), \mathbf{z}_1^{\gamma+1}, \mathbf{z}_2, \boldsymbol{\mu}_1^\gamma, \boldsymbol{\mu}_2^\gamma)$ , and, to attain that goal, it can be verified that the following condition always holds:

$$\mathbf{0} \in \mathbf{Q}\boldsymbol{\omega}_1^{\gamma+1} + \boldsymbol{\omega}_2^{\gamma+1}, \tag{28}$$

indicating that  $\boldsymbol{\omega}_1^{\gamma+1}$  and  $\boldsymbol{\omega}_2^{\gamma+1}$  satisfy (26) all the time. Furthermore, the dual residual, after a few mathematical derivations, is yielded to be

$$\begin{aligned} \zeta_3^{\gamma+1} &= -(\boldsymbol{\omega}_1^\gamma - \mathbf{Q}^H(\mathbf{z}_2^{\gamma+1} - \mathbf{z}_2^\gamma)) \\ \zeta_4^{\gamma+1} &= -\rho\left((\mathbf{z}_2^{\gamma+1} - \mathbf{z}_2^\gamma) - (\boldsymbol{\omega}_2^{\gamma+1} - \boldsymbol{\omega}_2^\gamma)\right). \end{aligned} \tag{29}$$

The termination criterion is employed as follows:

$$(\|\zeta_1^\gamma\|_2^2 + \|\zeta_2^\gamma\|_2^2)^{\frac{1}{2}} \leq \epsilon^{pri} \quad \text{and} \quad (\|\zeta_3^\gamma\|_2^2 + \|\zeta_4^\gamma\|_2^2)^{\frac{1}{2}} \leq \epsilon^{dual}, \tag{30}$$

where  $\epsilon^{pri}$  and  $\epsilon^{dual}$  are feasibility tolerances for the primal and dual feasibility conditions (25) and (26), respectively. These tolerances are designed to vary with iterations such as

$$\begin{aligned} \epsilon^{pri} &= \sqrt{\mathcal{L}_\rho}\epsilon^{abs} + \epsilon^{rel} \max\{\|\mathbf{z}_1^\gamma\|_2, \|\mathbf{Q}^H\bar{\mathbf{y}}_f(p)\|_2, \|\mathbf{Q}^H\mathbf{z}_2^\gamma\|_2\} \\ \epsilon^{dual} &= \sqrt{\mathcal{L}_\rho}\epsilon^{abs} + \epsilon^{rel}(\|\rho\boldsymbol{\omega}_1^\gamma\|_2^2 + \|\rho\boldsymbol{\omega}_2^\gamma\|_2^2)^{\frac{1}{2}}, \end{aligned} \tag{31}$$

where an absolute and relative criterion is used for adapting feasibility tolerances. The absolute tolerance  $\epsilon^{abs}$  is set to be  $10^{-4}$  whereas the relative stopping criterion  $\epsilon^{rel}$  is chosen at  $10^{-2}$  in the following simulations.

It is worth noting that setting the parameter value of  $\lambda$  in (17)—while attempting to minimize the  $\ell_1$ -norm of impulse noise estimate  $\tilde{\mathbf{i}}(p)$ —critically impacts the governance of clipping,

which in turn affects the BER performance. The optimal value of  $\lambda$  can however be empirically searched as this compressive sensing-based receiver, serving as a benchmark receiver, assumes not only the SNR level but also the statistics of impulse noise as well.

### 3 Neural Network Receiver

In this research endeavor, we emphasize harnessing the potential of artificial intelligence for the development of DNN-based receivers, eliminating the need to assume the prior knowledge of impulse noise models, related statistics, or SNR levels. This approach obviates the need to assume impulse noise models, associated statistics, or SNR levels. The subsequent section will provide an elaborate account of the architecture of our enhanced OFDM model, complete with pertinent mathematical representations. By capitalizing on proliferative training data generated through simulation processes, the DNN model is trained by treating OFDM modulation, multipath fading channels, and impulse noise as black boxes. Ultimately, the DNN model demonstrates its capability to effectively recover binary data sequences in real-world scenarios. The efficacy of this novel approach is substantiated by a meticulous comparative analysis, specifically evaluating the BER performance of our designed DNN-based receiver against a benchmark counterpart. Section 4 elaborates on the detailed insights of this assessment through the presentation of experimental outcomes

The DNN architecture comprises an input layer, multiple hidden layers, and an output layer, where neurons are fully connected between consecutive layers. The activation function employed at the output of the preceding hidden layer is the Rectified Linear Unit (ReLU) function, mathematically represented as follows:

$$\text{ReLU}(x) = \max(0, x). \quad (32)$$

Remarkably, the ReLU operation bears resemblance to soft thresholding, a technique commonly employed in signal processing and optimization tasks. This similarity becomes apparent, especially when disregarding the implicit sign implementation in (20), highlighting the intriguing connection between deep learning and signal processing paradigms. The Sigmoid function, serving as the nonlinear activation function at the output layer, is expressed as

$$\sigma(x) = \frac{1}{1 + e^{-x}}. \quad (33)$$

Referring to the weight matrix connecting the  $i$ -th and  $(i + 1)$ -th layers as denoted by  $\theta_{i+1,i}^{(s)}$ , the output of the  $(i + 1)$ -th layer is formulated as follows:

$$\mathbf{u}_{i+1}^{(s)} = f^{(i)}\left(\theta_{i+1,i}^{(s)} \mathbf{u}_i^{(s)}\right), \quad i \in \{1, 2, \dots, L_D - 1\} \text{ and } s \in \{1, 2, \dots, N_s\}, \quad (34)$$

where  $\mathbf{u}_i^{(s)}$  signifies the input of the  $i$ -th layer,  $L_D$  denotes the total number of layers in the DNN, and  $N_s$  represents the number of sub-systems. Figure 2 provides a visual representation where the DNN encompasses a total of five layers, with three hidden layers and eight sub-systems. It is noteworthy that each of these eight sub-systems processes identical received samples (following the removal of Cyclic Prefix) which spans a temporal duration equivalent to twice the length of an OFDM block, as input. Utilizing the notation delineated in (34), this alignment is denoted as  $\mathbf{u}_1^{(1)} = \mathbf{u}_1^{(2)} = \dots = \mathbf{u}_1^{(8)}$ , indicating the synchrony in their input sources. Furthermore, the activation functions  $f^{(i)}(\cdot)$ , where

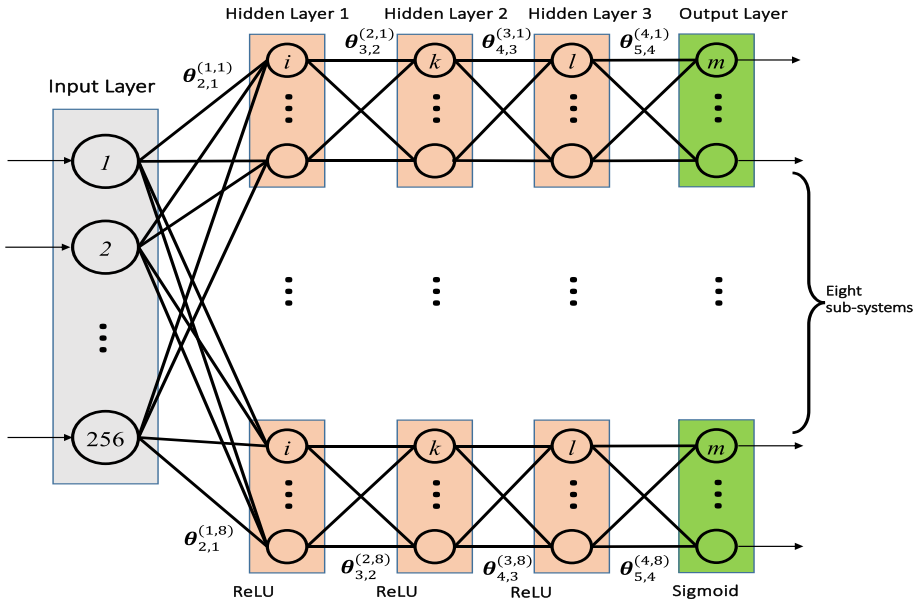


Fig. 2 DNN model

$i \in \{1, \dots, L_D - 2\}$ , are element-wise ReLU (32), while  $f^{(L_D-1)}(\cdot)$  employs the element-wise Sigmoid function. Finally, the collective vector  $[(\mathbf{u}_{L_D}^{(1)})^T (\mathbf{u}_{L_D}^{(2)})^T \dots (\mathbf{u}_{L_D}^{(N_s)})^T]^T$ , namely the output of the DNN, represents the estimation of the transmitted OFDM data block. The parameter set for which the DNN is trained, optimizing the specified metric (as detailed in the following passage), is succinctly summarized as  $\{\theta_{i+1,i}^{(s)}\}$ , where  $i \in \{1, 2, \dots, L_D - 1\}$ , and  $s \in \{1, 2, \dots, N_s\}$ .

In contrast to the employed mean-squares error (MSE) loss function, namely  $L_2 = \sum_{k=1}^{N_{train}} \|\hat{\mathbf{X}}^{(k)} - \mathbf{X}^{(k)}\|_2^2 / N_{train}$  as employed in [32], where  $N_{train}$  represents the scale of the training dataset,  $\hat{\mathbf{X}}^{(k)}$  signifies the prediction generated by our proposed DNN, and  $\mathbf{X}^{(k)}$  indicates the ground truth corresponding to training dataset  $k$ , we opt for the cross-entropy loss function as the focal point of the cost function in this paper. The choice of the cross-entropy loss function is motivated by its suitability for classification tasks, as underscored in prior research [9]. Additionally, our simulation results, as presented in the following, validate its superiority—particularly when faced with instances of unforeseen impulse noise occurrences.

For the sake of conciseness and notational clarity, we omit the superscript  $(k)$  which corresponds to the training dataset index in the subsequent discussions. The ultimate layer, which is fully connected, directs crucial output information to an In-phase and Quadrature-phase (I/Q) softmax layer. This specialized layer computes probabilities for each transmitted two-bit binary partition and adopts a vector configuration (specifically, a four-by-one vector), as elaborated in the ensuing description:

$$[P((\hat{\mathbf{u}}_m)_1 = 1) \ P((\hat{\mathbf{u}}_m)_1 = 0) \ P((\hat{\mathbf{u}}_m)_2 = 1) \ P((\hat{\mathbf{u}}_m)_2 = 0)]^T. \tag{35}$$

In the context of QPSK modulation demapped using Gray mapping, the probabilities associated with the I/Q components can be derived from the aforementioned equation (35), presented here in the subsequent vectorized form:

$$\left[ P\left(\Re\{\hat{X}_m\} = \frac{-E_s}{\sqrt{2}}\right) P\left(\Re\{\hat{X}_m\} = \frac{E_s}{\sqrt{2}}\right) P\left(\Im\{\hat{X}_m\} = \frac{-E_s}{\sqrt{2}}\right) P\left(\Im\{\hat{X}_m\} = \frac{E_s}{\sqrt{2}}\right) \right]^T. \quad (36)$$

Guided by standard practices, the process of normalization ensures that the subsequent summations attain a unity value:  $P((\hat{\mathbf{u}}_m)_1 = 1) + P((\hat{\mathbf{u}}_m)_1 = 0) = 1$ , and similarly,  $P((\hat{\mathbf{u}}_m)_2 = 1) + P((\hat{\mathbf{u}}_m)_2 = 0) = 1$ . In the context of each trained OFDM block, the adeptness of our DNN model in minimizing the cross-entropy loss function is succinctly demonstrated, as articulated in the subsequent expression:

$$L_c = -\frac{1}{N} \sum_{m=0}^{N-1} \sum_{q=0}^1 [\mathbb{1}((\mathbf{u}_m)_1 = q) \log P((\hat{\mathbf{u}}_m)_1 = q) + \mathbb{1}((\mathbf{u}_m)_2 = q) \log P((\hat{\mathbf{u}}_m)_2 = q)]. \quad (37)$$

Derived from the cross-entropy loss function  $L_c$  outlined in (37), the evolution of the weights and biases within the DNN model transpires through the realization of a stochastic gradient descent method, or its relevant extension, operating on incoming batches of the training dataset. The initial phase of training the DNN model is characterized by the pursuit of minimizing the loss function  $L_c$ , amid the presence of data-corrupting interference solely attributed to AWGN.

However, in response to the challenge posed by non-Gaussian impulse noise, this study, following the lead of [14], undertakes a refinement of the previously established DNN model. This evolution involves strategically interleaving the training data with instances of impulse noise subsequent to the initial training phase. This strategic interleaving enables the systematic fine-tuning of the parameters of the DNN model. This iterative process continues until the value of the loss function (37) reaches a point of marginal diminishment, indicating the enhanced robustness of the proposed DNN model to non-Gaussian disturbances.

It is noteworthy that the learning rate, which is subject to experimentation in the subsequent section, is deliberately decreased over the course of training. This deliberate reduction in the learning rate is driven by the objective of attaining convergence toward an optimal solution within the intricate domain of DNN modeling, wherein the interplay between model complexity and convergence efficiency is meticulously balanced.

## 4 Simulation Results

The simulations adopt the B-G and SaS impulse noise models (as described in Sect. 2.2). In contrast to previous studies, such as the work in [28], we vary the IGR within the range of SNR values relevant to our investigation. The DNN's input consists of received data from a frame, comprising one pilot block and one data block. Each block contains 64 QPSK symbols, aligned with an FFT/IFFT size of  $N = 64$ . The pilot symbols remain fixed during training and validation. As in [32], the CP length is set to  $\mathcal{L}_p = 16$ . Moreover, the wireless channel dataset is generated following the new radio model (WINNER II [16]), resulting in a multipath channel with 24 paths, which varies from one frame to another. Notably, the received signal, conditioned on channel gains  $h_k^{(i)}$ , where  $k \in \{0, 1, \dots, L-1\}$ , derived from the  $i$ -th channel realization, where  $i \in \{1, 2, \dots, N_d\}$ , in a dataset of size  $N_d$ , follows a Gaussian distribution with a mean of zero and a variance of

$\sigma_{r_i}^2 = \left( \sum_{k=0}^{L-1} |h_k^{(i)}|^2 \right) E_s$ . In this regard, signal-to-Noise ratio (SNR) is defined as the ratio of the averaged received signal power over the dataset of interest to the variance of AWGN, namely  $(\frac{1}{N_d} \sum_{i=1}^{N_d} \sigma_{r_i}^2) / N_0$ . SNR values are expressed in decibels (dB) for the following simulations. It is pivotal to highlight that while the compressive sensing-based receiver leverages channel state information and AWGN power levels to generate BER curves, our DNN-based receiver operates without presuming any prior knowledge of these parameters.

Figure 3 presents the BER performance outcomes of the trained model, building upon experiments from [32]. In contrast to their study, which focused exclusively on AWGN, we extend our investigation to incorporate moderate impulse noise, characterized by a probability of impulse occurrence  $p_b = 0.001$  with variances ranging from 0.02 to 2.5. The DNN model is composed of five layers, with neurons allocated as follows: 256, 500, 250, 120, and 16. Notably, every 16 bits of the transmitted data are independently predicted prior to concatenation as a whole (128 bits.) Training involves 5,000 epochs, each comprising 50 batches (with 500 training realizations per batch). We employed the Adam optimizer [15] with a learning rate of  $10^{-4}$ . For specific system parameter values, please refer to Table 1. Analyzing Fig. 3 reveals that as  $\sigma_I^2$ , representing impulse noise power, grows, the BER performance stabilizes at lower SNR values; for instance, at  $\sigma_I^2 = 2.5$ , the BER curve becomes notably flat from as early as 15-dB SNR. Conversely, the curve for  $\sigma_I^2 = 0.02$  exhibits gradual tilting. However, even in the latter scenario—moderate impulse probability coupled with minimal power intensity—the BER remains significantly higher than  $10^{-3}$ . This performance gap persists even as SNR ascends to 30 dB (see solid line marked by “□”). Our experimental insights underscore a critical point: although the trained model excels in the presence of AWGN only—where the BER declines to less than  $10^{-3}$  at SNR levels below 30 dB—its effectiveness diminishes when faced with the unforeseen presence of impulse noise. This observation highlights the formidable challenge of mitigating the impact of impulse noise without enhancements to the model. Notably, the dash-dotted line

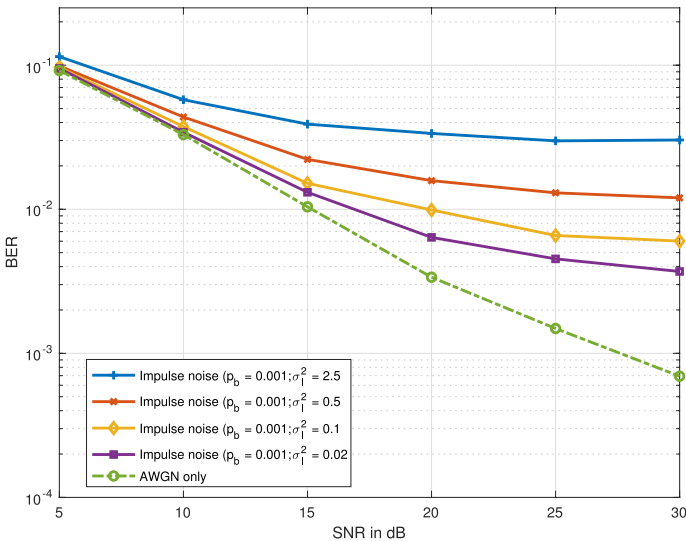


**Fig. 3** BER performance of the DNN model (trained in the context of AWGN only) in the B-G model ( $p_b = 0.001$ )

marked by “o” aligns with findings in [32], revealing BER performance comparable to that of the MMSE receiver.

In response to this shortcoming, we adopt a successive fine-tuning approach for the trained model parameters. This strategy is employed once the value of the loss function (37) has reached a plateau, and no further decline can be achieved by increasing the number of training epochs. In our study, this point is observed at 5,000 epochs. Beginning with the model parameters obtained from the initial structure, this enhanced method yields a refined DNN model through fine-tuning. This process occurs at a fixed training SNR level of 25 dB.

The fine-tuning process incorporates the following key adjustments: the learning rate is reduced to one-fifth of its most recent value after every 25 epochs, eventually reaching a minimum value of  $10^{-5}$ . Simultaneously, the training dataset, distinct from the previous experiment, considers impulse occurrences with a probability set at 0.005 and an average power of 0.2. The outcomes of these refinements under error-prone conditions are displayed in Fig. 4. In comparison to the original DNN model, the BER curves derived from the incorporation of fine-tuning (indicated by solid lines) exhibit an earlier descent than their counterparts (represented by dash-dotted lines) across a comprehensive range of  $\sigma_I^2$  strengths. For instance, considering the instance where  $\sigma_I^2 = 0.02$  (highlighted by “□” on the curves),

a noteworthy SNR improvement of over 10 dB is evidenced. This observation underscores the affirmative impact of incorporating the fine-tuning technique into the DNN model. The discerned superiority of the refined DNN model over the original version can be attributed to the transfer of knowledge from the pre-trained model—leveraging learned parameters as initializations—which is then subjected to fine-tuning for tackling more intricate learning tasks, such as addressing anomalous attacks.

Furthermore, the receiver employing clipping (indicated by the dashed line marked with “o” in Fig. 4), with an optimal threshold determined via linear programming (as discussed in Sect. 2.3) through an exhaustive exploration of the parameter  $\lambda$  in (16),

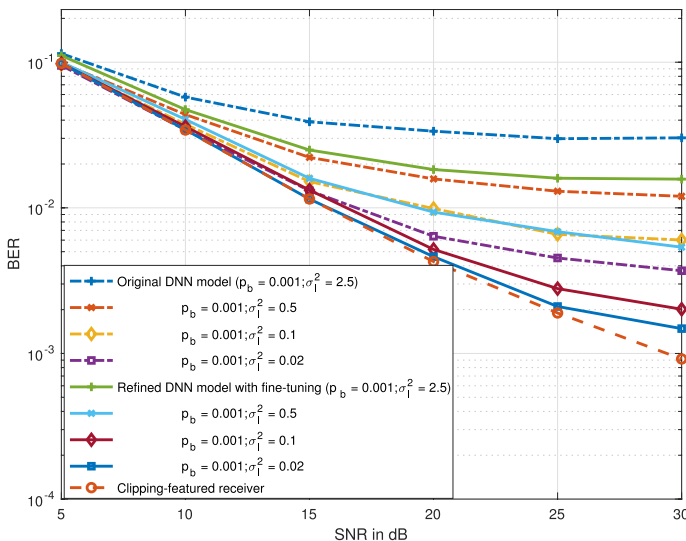


Fig. 4 BER performance of the refined DNN model (with fine-tuning) in the B-G model ( $p_b = 0.001$ )



slightly outperforms the refined DNN-based receiver. However, it is worth noting that the clipping-featured receiver necessitates the assumption of known SNR values. In contrast, the refined DNN receiver does not assume knowledge of the impulse noise statistics or SNR values from the testing data.

Notably, even under relatively mild conditions, such as  $p_b = 0.001$  and  $\sigma_I^2 = 0.02$ , the achieved BER performance in the preceding experimental findings reaches a saturation point around 30-dB SNR. This is particularly significant when considering the instances where  $p_b$  is substantially elevated, highlighting the limitations of the preceding DNN model. This issue is prominently depicted in Fig. 5, where the DNN model encounters heightened instances of anomalous occurrences, notably at  $p_b = 0.01$  across the entire range of presented  $\sigma_I^2$  magnitudes. This is observable through the consistent BER levels (indicated by the dash-dotted lines) that persist even as the SNR value surpasses 25 dB. This behavior indicates that the DNN-based receiver becomes overwhelmed by the influx of impulse arrivals within the data frame duration.

To overcome this shortcoming, we enhance the DNN model by augmenting the network depth from five to six layers. Additionally, we meticulously determine the number of neurons in each layer empirically as follows: 256, 550, 832, 280, 128 and 16. The fine-tuning process remains consistent with the strategy outlined earlier. The resulting BER outcomes are depicted in Fig. 5, with each solid line corresponding to a distinct  $\sigma_I^2$  level. A noteworthy observation emerges: the lower the average power of the impulse noise, the earlier the departure of BER curves between the two compared DNN models as the SNR grows. Strikingly, for  $\sigma_I^2$  values of 0.1 and 0.02, the 'deeper' neural network model induces a consistent downward trajectory of BER curves as SNR progressively increases.

Of notable significance, the BER performance achieved remarkably converges with outcomes obtained from the clipping-featured receiver (as indicated by the dashed line marked by "o"), attesting the efficacy of our proposed DNN framework against impulse noise,

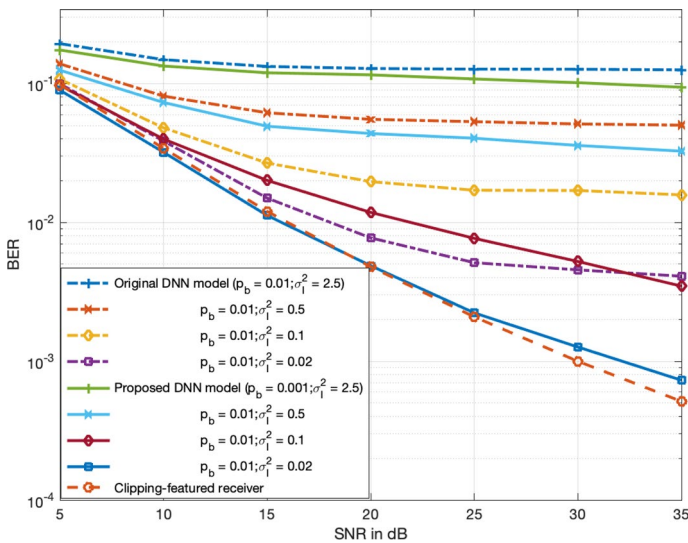
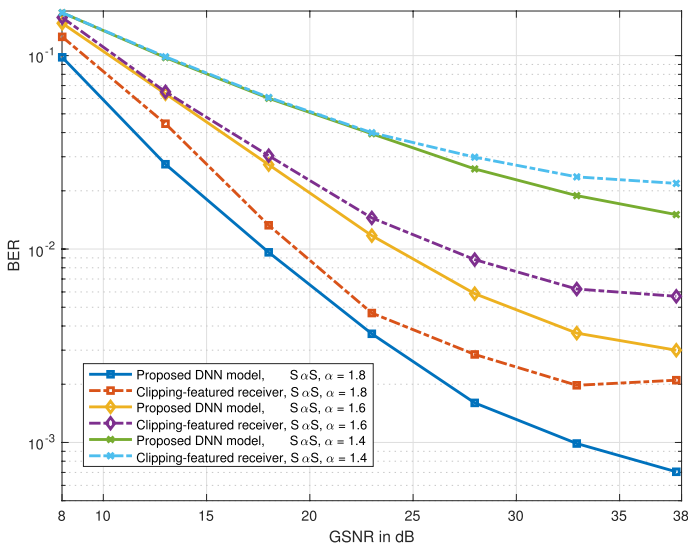


Fig. 5 BER performance of the proposed DNN model (with fine-tuning) in the B-G model with a growing  $p_b$  at 0.01

even in hostile scenarios. In summation, this notable performance enhancement is adapted through a strategic trade-off, judiciously balancing computational complexity to enrich the prowess of representation learning.

To further amplify the robustness claims of our proposed DNN-based receiver—relaxing its assumptions on the specifics of the driving impulse noise model—we carry out a pivotal experiment. In this experiment, we intentionally replace the interference model in the testing phase with the symmetric alpha-stable distribution (as defined in (9)), thereby introducing a deliberate model mismatch. This strategic maneuver investigates the efficacy of the receiver in the face of variations stemming from the impulsiveness of interference. This exploratory path involves a meticulous modulation of the magnitude of the  $\alpha$  parameter, as delineated in (10). Specifically, we scrutinize the outcomes for varying values of  $\alpha$ , specifically 1.4, 1.6, and 1.8, throughout our simulations, as detailed below. Notably, the performance outcomes detailed within Fig. 6 unequivocally resonate with our central assertion: the devised DNN model consistently outperforms its counterpart. This superiority becomes particularly evident as the performance loss incurred by the clipping-featured receiver—developed based on assuming the Gaussian mixture noise model—becomes substantial due to its susceptibility to a model mismatch. The stark divergence from the assumed  $S\alpha S$  model becomes an essential factor responsible for this phenomenon. This disparity is acutely illustrated when considering an instance with  $\alpha$  set at 1.8: the BER performance curve dictated by the clipping-featured receiver (as denoted by the dash-dotted line marked by “□”) exhibits minimal downward movement, starkly contrasting with the trajectory observed with our proposed DNN model. As the BER derived from our DNN receiver steadily declines amidst growing G SNR values, the gap in performance loss with regard to the clipping-featured counterpart magnifies significantly.

In pursuit of a comprehensive assessment, we extend our evaluation by comparing our DNN-based receiver with a peer model proposed in [2], which enhances performance



**Fig. 6** BER performance comparison of the trained DNN model (with fine-tuning) and a clipping-featured receiver in realistic scenarios in the presence of model mismatch, where  $\alpha$  values in the  $S\alpha S$  model are varied

through the integration of convolutional coding. To facilitate a thorough, equitable comparative analysis, we conduct simulations within a coded OFDM framework encompassing 1,024 sub-carriers, out of which 256 are dedicated to pilots. The code rate is set at 1/2, with a constraint length of 7 and generator matrix defined by [171 133]. Channel decoding is implemented via a Viterbi decoder. Further augmenting the simulation settings is the channel model, which comprises ten paths with path arrival times conforming to a Poisson distribution with a mean of 1 ms, whereas the path amplitudes follow the Rayleigh fading distribution, reflecting an exponentially decreasing average power profile. It is noteworthy that the same strategy is employed, enabling the retraining of our proposed DNN to adapt to the unique characteristics of this channel model. The performance disparity between our DNN receiver and the counterpart in [2], within the B-G model, is depicted in Fig. 7. Notably, across all scenarios, the divergence between comparative curves becomes more pronounced as the SNR value grows. A discernible 0.5 dB SNR gain (see those lines marked by “x”) is observed at a BER level of  $10^{-4}$  when  $p_b = 0.06$ . Their performance loss can be attributed to the quality of channel estimation—a crucial factor impacting zero-forcing frequency domain equalization, known for its susceptibility to noise enhancement. This is corroborated by our observation that the solid line representing our DNN-based receiver consistently falls below the dash-dotted line, even when limited to the AWGN scenario (marked by “□”). The impact of adopting blanking operation there in scenarios with higher  $p_b$  values, such as 0.1, can further contribute to a degraded BER performance.

Our exploration further extends to the MC-A model, the outcomes of which are plotted in Fig. 8. The BER performance aligns with the trends exhibited in Fig. 7. Particularly notable is its marginal yet consistent superiority compared to the counterpart across various impulsive indices  $A$ , especially when the power ratio between AWGN and moderate impulse noise remains constant (e.g.,  $\Lambda = 0.5$ ). This persistence in performance gain further solidifies the versatility and efficacy of our DNN-based receiver across diverse impulsive environments.

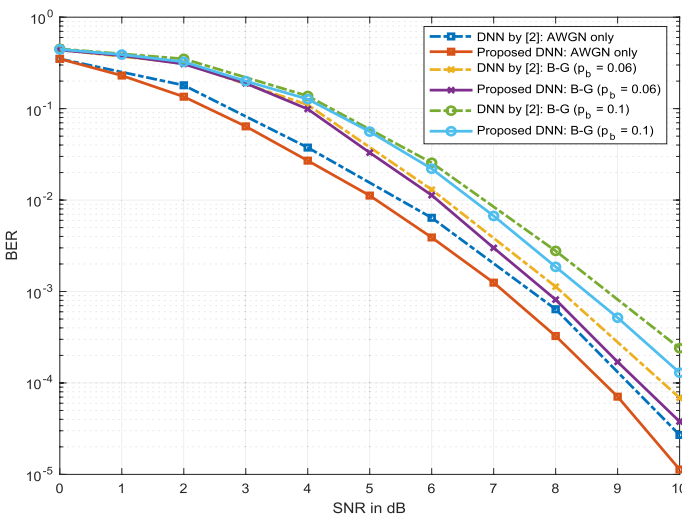
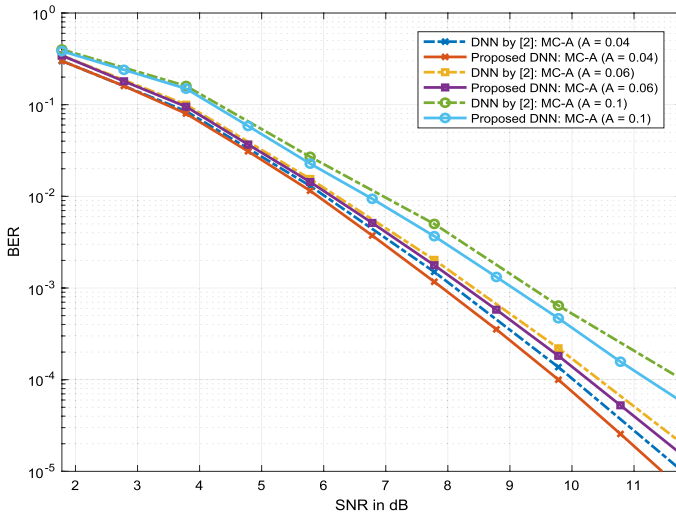


Fig. 7 BER performance comparison of the trained DNN model with the one proposed in [2] at SIR = 0 dB



**Fig. 8** BER performance comparison of the trained DNN model with the one proposed in [2] in the MC-A model with  $\Lambda = 0.5$

**Table 1** The hyperparameters of the DNN

Parameter	Value
Activation function	ReLU
Loss function	Cross entropy
Epoch index	AWGN: 1–2000/ with impulse noise: 2001–5000
Batch number per epoch	50
Training set of each batch	500
Bits of each training set	128
Initialization method	Xavier initialization
Learning rate	Initialized at 0.001 and continually shrunk to be 1/5 of its latest value after every 25 epochs
Optimization method	Adam
Power level of AWGN in training mode	$5.45 \times 10^{-5}$
Probability of impulse noise occurrence in training mode	0.001
Power level of impulse noise in training mode	2

## 5 Conclusion

In summary, we have delved into the formidable implications of impulse noise on the bit error rate (BER) performance of a deep neural network (DNN) receiver tailored for Orthogonal Frequency Division Multiplexing systems in the presence of multipath fading. Notably, our study encompasses a scenario where the precise impulse noise statistics remain elusive to the DNN receiver, mirroring real-world uncertainties, and extends to instances where the ambient noise power level remains uncharted. Empirical

revelations emphasize the vulnerability of a DNN model exclusively trained to contend with additive white Gaussian noise, rendering it susceptible to the covert yet detrimental anomalies introduced by impulse occurrences. Consequently, a critical facet of this study emerges—enriching the DNN’s capacity for representation learning by enabling adaptive responses to nuanced data variations, effectively rejuvenating the initial training model. In this endeavor, the prominent clipping-featured receiver, emanating from the compressive sensing paradigm, emerges as a pertinent benchmark for BER performance comparison against our DNN receiver. Of paramount significance, our investigation unveils a pivotal nexus between optimal clipping thresholds—a cornerstone of the compressive sensing-based clipping-featured receiver—and the efficient resolution of this task through a second-order cone programming realized by the consensus alternating direction method of multipliers (ADMM). Nonetheless, it is imperative to acknowledge that the conventional clipping-featured receiver’s efficacy in setting the clipping threshold is engaged with an assumption about the signal-to-noise ratio level—a presumption that our proposed DNN receiver manages to circumvent. Our simulation results elegantly demonstrate the prowess of the proposed DNN receiver, aligning it commendably with its clipping-featured peer in moderate environments and even surpassing it slightly in more hostile scenarios. Moreover, our DNN receiver underscores robustness in the face of impulse noise model mismatches, further attesting to its practicality and adaptability.

**Acknowledgements** The authors acknowledged the research funding received from the Ministry of Science and Technology (MOST) of Taiwan for the major research projects.

**Author Contributions** D-FT, the corresponding author, contributed to the study conception, performed system design and experiments, and wrote the first draft of the manuscript. C-SL conducted computer simulations. S-MT made significant contributions to the analysis and conception of the study. All authors read and approved the final manuscript.

**Funding** This work was supported by the Ministry of Science and Technology (MOST) of Taiwan under grant no. MOST 109-2221-E-011-119-, MOST 110-2221-E-011-066- and MOST 111-2221-E-011-060 -.

**Data Availability** Data are available upon request.

## Declarations

**Conflict of interest** The authors declare that they have no competing interests.

**Ethical Approval and Consent to Participate** This article does not contain any studies with human participants or animals performed by any of the authors and all authors have read and understood the provided information.

**Consent for Publication** This article does not contain any images or videos to get permission and all authors gave consent for publication.

## References

1. Al-Naffouri, T. Y., Quadeer, A. A., & Caire, G. (2014). Impulse noise estimation and removal for OFDM systems. *IEEE Transactions on Communications*, 62(3), 976–989.
2. Barazideh, R., Niknam, S., & Natarajan, B. (2019). Impulsive noise detection in OFDM-based systems: A deep learning perspective. In *Proceedings of the IEEE 9th annual computing and communication workshop and conference (CCWC 2019)* (pp. 937–942).

3. Boyd, S., Parikh, N., Chu, E., Peleato, B., & Eckstein, J. (2011). Distributed optimization and statistical learning via the alternating direction method of multipliers. *Foundations and Trends in Machine Learning*, 3, 1–122.
4. Candes, E. J., & Randall, P. A. (2008). Highly robust error correction by convex programming. *IEEE Transactions on Information Theory*, 54(7), 2829–2840.
5. Ferrer-Coll, J., Slimane, S., & Chilo, J. E. A. (2015). Detection and suppression of impulsive noise in OFDM receiver. *Wireless Personal Communications*, 85, 2245–2259. <https://doi.org/10.1007/s11277-015-2902-4>
6. Fesl, B., Turan, N., Joham, M., & Utschick, W. (2023). Learning a Gaussian mixture model from imperfect training data for robust channel estimation. *IEEE Wireless Communications Letters*, 12(6), 1066–1070.
7. Gao, X., Jin, S., Wen, C. K., & Li, G. Y. (2018). ComNet: Combination of deep learning and expert knowledge in OFDM receivers. *IEEE Communications Letters*, 22(12), 2627–2630.
8. Ghosh, M. (1996). Analysis of the effect of impulse noise on multicarrier and single carrier QAM systems. *IEEE Transactions on Communications*, 44(2), 145–147.
9. Glorot, X., & Bengio, Y. (2010). Understanding the difficulty of training deep feedforward neural networks. In *Proceedings of the international conference on artificial intelligence and statistics (AISTATS)* (pp. 249–256).
10. Gonzalez, J. G., Paredes, J. L., & Arce, G. R. (2006). Zero-order statistics: A mathematical framework for the processing and characterization of very impulsive signals. *IEEE Transactions on Signal Processing*, 54(10), 3839–3851.
11. Goodfellow, I. J., Shlens, J., & Szegedy, C. (2014). Explaining and harnessing adversarial examples. [arXiv:1412.6572](https://arxiv.org/abs/1412.6572)
12. Grant, M., & Boyd, S. (2014). CVX: Matlab software for disciplined convex programming, version 2.1.1. <http://cvxr.com/cvx>
13. He, Y., Zou, C., Li, D., Yao, R., Yang, F., & Song, J. (2023). Adaptive impulsive noise suppression: A deep learning-based parameters estimation approach. *IEEE Transactions on Broadcasting*, 69(2), 505–515.
14. Kim, H., Oh, S., & Viswanath, P. (2020). Physical layer communication via deep learning. *IEEE Journal on Selected Areas in Information Theory*, 1(1), 5–18.
15. Kingma, D., & Ba, J. (2015). Adam: A method for stochastic optimization. In *Proceedings of the 3rd international conference on learning representations*.
16. Kyosti, P., et al. (2007). Winner II channel models. Eur. Commission, Brussels, Belgium, Tech. Rep. D1.1.2 IST-4-027756-WINNER.
17. Li, J., Zhang, Z., Wang, Y., He, B., Zheng, W., & Li, M. (2023). Deep learning-assisted OFDM channel estimation and signal detection technology. *IEEE Communications Letters*, 27(5), 1347–1351.
18. Li, X., Han, Z., Yu, H., Yan, L., & Han, S. (2022). Deep learning for OFDM channel estimation in impulsive noise environments. *Wireless Personal Communications*, 125, 2947–2964. <https://doi.org/10.1007/s11277-022-09693-z>
19. Mandal, A. K., & De, S. (2023). A novel learning-based estimation scheme for communication over impulsive noise channels. *IEEE Wireless Communications Letters*, 12(7), 1154–1158.
20. Middleton, D. (1983). Canonical and quasi-canonical probability models of Class A interference, (pp. 76–106).
21. Mulla, M., Rizaner, A., & Ulusoy, A. (2022). Fuzzy logic based decoder for single-user millimeter wave systems under impulsive noise. *Wireless Personal Communications*, 124, 1883–1895. <https://doi.org/10.1007/s11277-021-09435-7>
22. Nikias, C. L., & Shao, M. (1995). *Signal processing with alpha-stable distributions and applications*. Wiley.
23. O’Shea, T. J., & Hoydis, J. (2017). An introduction to deep learning for the physical layer. *IEEE Transactions on Cognitive Communications and Networking*, 3(4), 563–575.
24. Selim, B., Alam, M. S., Evangelista, J. V. C., Kaddoum, G., & Agba, B. L. (2020). NOMA-based IoT networks: Impulsive noise effects and mitigation. *IEEE Communications Magazine*, 58(11), 69–75.
25. Selim, B., Alam, M. S., Kaddoum, G., AlKhodary, M. T., & Agba, B. L. (2020). A deep learning approach for the estimation of Middleton Class-A impulsive noise parameters. In *IEEE international conference on communications* (pp. 1–6).
26. Shi, J., Lu, A. A., Zhong, W., Gao, X., & Li, G. Y. (2023). Robust WMMSE precoder with deep learning design for massive MIMO. *IEEE Transactions on Communications*, 71(7), 3963–3976.
27. Tsai, T. R., & Tseng, D.-F. (2008). Subspace algorithm for blind channel identification and synchronization in single-carrier block transmission systems. *Signal Processing*, 88(2), 296–306.

28. Tseng, D.-F., Han, Y. S., Mow, W. H., Chang, L. C., & Vinck, A. J. H. (2012). Robust clipping for OFDM transmissions over memoryless impulsive noise channels. *IEEE Communications Letters*, 1110–1113.
29. Tseng, D.-F., & Lin, C. S. (2021). A study of neural network receivers in OFDM systems subject to memoryless impulse noise. In *Proceedings of the 30th Wireless and Optical Communications Conference (WOCC2021)* (pp. 16–20).
30. Tseng, S.-M., Hsu, W. C., & Tseng, D.-F. (2022). Deep learning based decoding for polar codes in Markov Gaussian memory impulse noise channels. *Wireless Personal Communications*, 122, 737–753. <https://doi.org/10.1007/s11277-021-08923-0>
31. Xiao, M., et al. (2017). Millimeter wave communications for future mobile networks. *IEEE Journal on Selected Areas in Communications*, 35(9), 1909–1935.
32. Ye, H., Li, G. Y., & Juang, B. (2018). Power of deep learning for channel estimation and signal detection in OFDM systems. *IEEE Wireless Communications Letters*, 7(1), 114–117.
33. Zhao, H., Yang, C., Xu, Y., Ji, F., Wen, M., & Chen, Y. (2023). Model-driven based deep unfolding equalizer for underwater acoustic OFDM communications. *IEEE Transactions Vehicular Technology*, 72(5), 6056–6067.

**Publisher's Note** Springer Nature remains neutral with regard to jurisdictional claims in published maps and institutional affiliations.

Springer Nature or its licensor (e.g. a society or other partner) holds exclusive rights to this article under a publishing agreement with the author(s) or other rightsholder(s); author self-archiving of the accepted manuscript version of this article is solely governed by the terms of such publishing agreement and applicable law.



**Der-Feng Tseng** received his B.S.E.E. degree from National Chiao Tung University, Taiwan, and M.S.E.E. and Ph.D. degrees from Purdue University, West Lafayette, Indiana. He was with TRW-ESL, Sunnyvale, CA, and Motorola Mobility, Piscataway, NJ, as Senior Systems Engineer engaged in embedded software development for mobile devices before joining National Taiwan University of Science and Technology, where he has been with since February 2003. He was a visiting research scholar in the Department of Electrical Engineering at the University of Houston from June to September 2013. He was the coreipient of “The Fred Ellersick MILCOM Award for Best Paper in the Unclassified Technical Program” at the IEEE MILCOM’98, Boston, MA. His research interests lie in the areas of communication systems, machine learning, statistical signal processing, and channel coding techniques.



**Che-Shien Lin** received the M.S. degree in electrical engineering from the Department of Electrical Engineering, National Taiwan University of Science and Technology, Taipei, Taiwan, in 2021. He is currently with Realtek Semiconductor Corporation, Hsinchu, Taiwan. His research interests include LDPC coding, B5G transmission technology, signal processing techniques for communication systems, and deep learning.



**Shu-Ming Tseng** received the Ph.D. degree in electrical engineering from Purdue University, West Lafayette, IN, USA, in 1999. Since 2001, he has been with the Department of Electronic Engineering, National Taipei University of Technology, Taipei, Taiwan, where he has been a Professor since 2007. He is the author of 58 SCI journal papers, including 17 in IEEE. His research interests include AI, B5G, radio-resource allocation, cross-layer design, video temporal segmentation, network performance evaluation, and optical sensors. He is the Editor of *KSII Transactions on Internet and Information Systems*. He was the TPC Co-Chair of IEEE 2021 30th Wireless and Optical Communications Conference, (WOCC 2021). He is a TPC Member of IEEE IWCMC 2022 LowPowerIoT Symposium.